BIOCHEMISTRY

Three-dimensional imaging and analysis of pathological tissue samples with de novo generation of citrate-based fluorophores

Jinyoung Pac[1]†, Dong-Jun Koo[2]†, Hyeongjun Cho[1,2], Dongwook Jung[1], Min-ha Choi[3], Yunjung Choi[1], Bohyun Kim[4]*, Ji-Ung Park[3]*, Sung-Yon Kim[1,2]*, Yan Lee[1]*

Two-dimensional (2D) histopathology based on the observation of thin tissue slides is the current paradigm in diagnosis and prognosis. However, labeling strategies in conventional histopathology are limited in compatibility with 3D imaging combined with tissue clearing techniques. Here, we present a rapid and efficient volumetric imaging technique of pathological tissues called 3D tissue imaging through de novo formation of fluorophores, or 3DNFC, which is the integration of citrate-based fluorogenic reaction DNFC and tissue clearing techniques. 3DNFC markedly increases the fluorescence intensity of tissues by generating fluorophores on nonfluorescent amino-terminal cysteine and visualizes the 3D structure of the tissues to provide their anatomical morphology and volumetric information. Furthermore, the application of 3DNFC to pathological tissue achieves the 3D reconstruction for the unbiased analysis of diverse features of the disorders in their natural context. We suggest that 3DNFC is a promising volumetric imaging method for the prognosis and diagnosis of pathological tissues.

INTRODUCTION

Histopathology is a microscopic analysis of the distribution and morphology of cells and tissue lesions. Microscopic examination of micrometer-thick tissue slides stained by hematoxylin and eosin (H&E) or Masson's trichrome staining methods has been used for over a hundred years to visualize pathological features of biological tissue specimens and has provided a solid basis for diagnosis and prognosis (*1*, *2*). However, it is difficult to understand the precise and detailed spatial progression of diseases in pathological tissue samples using only two-dimensional (2D) information from traditional histopathology, and the limited information, in some cases, may lead to incorrect diagnosis (*3*, *4*). Moreover, conventional histological stains are poorly compatible with the recently developed light microscopy–based volumetric imaging, owing to their absorbance-based staining properties (*5*). Thus, there is a growing demand for 3D information about pathologic lesions to improve our understanding of disease progression and the accuracy of histopathological examinations.

For fast and intact thick tissue imaging without tissue sectioning, tissue clearing techniques using a series of chemical treatments for homogenization of the refractive index (RI) to make tissues transparent have been introduced in recent years (*6*–*8*). Combined with fluorescence microscopy modalities resolving axial section images (e.g., confocal microscopy), tissue clearing techniques allow volumetric imaging of normal or histopathological samples at a single-cell resolution with high sensitivity, although they are not entirely free from the scattering issue of thick tissue samples (*9*–*16*). Staining with fluorescence-labeled antibodies provides spatial information of target biomolecules with excellent specificity; several organic fluorescent dyes with reactive functional groups have also been used to obtain the anatomical morphology of biological samples (*5*). However, each labeling method presents several challenges. Because of the relatively large molecular weight, fluorescence-labeled antibodies exhibit slow penetration of thick tissues (*17*, *18*). On the other hand, reactive organic dyes used in tissue staining are costly or produce false-positive readouts, owing to the nonspecific binding of fluorescent probes (*19*–*21*). Autofluorescence of biological tissues without fluorescence labeling has also been used to delineate tissue anatomy (*22*). However, because of the weak autofluorescence intensity of tissue samples, autofluorescence imaging requires a relatively strong excitation laser (*23*), which quenches other potentially useful fluorophores in the sample (*24*). To date, intact, effective, and uniform labeling and imaging techniques for thick tissue specimens have not been achieved, despite the need for imaging and volumetric analysis of thick tissues.

Here, we show an imaging technique for thick tissues termed 3DNFC ("3D tissue imaging through de novo formation of citrate-based fluorophores") that enables precise 3D reconstruction using a fluorogenic reaction on nonfluorescent biomolecules. Previously, citrate, a small hydrophilic tricarboxylic acid, was reported to react with cysteine to form a strong blue fluorophore, 5-oxo-2,3-dihydro-5H-[1,3]thiazolo[3,2-a]pyridine-3,7-dicarboxylic acid (TPA), through serial condensation and dehydration reactions at high temperature (*25*–*30*). Our group could facilitate fluorophore formation under mild reaction conditions by using amide coupling reagents for applications in biological samples (*31*). The DNFC reaction forms the TPA fluorophores rapidly under mild reaction conditions and is more cost-effective than staining methods using antibodies or fluorescent dyes. Furthermore, because of the low molecular weight of citrate, DNFC is expected to show enhanced penetration ability without aggregation by nonspecific interactions and produce uniform staining results for thick specimen labeling by forming fluorophores on proteins or peptides with N-terminal cysteines (*31*). Therefore, we developed the 3DNFC technique, the integration of 3DISCO

[1]Department of Chemistry, Seoul National University, Seoul 08826, South Korea. [2]Institute of Molecular Biology and Genetics, Seoul National University, Seoul 08826, South Korea. [3]Department of Plastic and Reconstructive Surgery, Seoul National University Boramae Hospital, Seoul National University College of Medicine, 5 Gil 20, Boramae Road, Dongjak-Gu, Seoul 07061, South Korea. [4]Department of Pathology, Konkuk University Medical Center, Konkuk University School of Medicine, Seoul, South Korea.
*Corresponding author. Email: gacn@snu.ac.kr (Y.L.); sungyonkim@snu.ac.kr (S.-Y.K.); alfbskan@gmail.com (J.-U.P.); bohyuncherish@gmail.com (B.K.)
†These authors contributed equally to this work.

["3D imaging of solvent-cleared organs" (*6*)], which is a representative tissue clearing technique, and DNFC staining for thick tissue imaging and volumetric analyses. We confirmed that 3DNFC successfully imaged various tissues and visualized the 3D structure of large volume tissue specimens from mice. In addition, we reconstructed the detailed structures of pathological tissues with nonalcoholic fatty liver disease (NAFLD) and human-derived breast cancer by 3DNFC. We analyzed the lesions quantitatively and qualitatively for diagnostic evaluation of complex pathological specimens. Together, we believe that 3DNFC can be applied as a new method in histology and histopathology, which allows precise 3D reconstruction and comprehensive spatial analysis of the wide variety of large-scale tissues through versatile tissue labeling and imaging.

RESULTS

Fluorophore generation in tissues and organs by 3DNFC

To achieve a uniform and accurate labeling of large-scale specimens, we used the DNFC. It has been reported that citrate can form TPA, a bright blue fluorophore, through a reaction with cysteine with heating at 100° to 180°C (*25*–*30*). However, we found that TPA can be formed in biological samples even at ambient temperature by adding the coupling reagent, PyBOP (benzotriazole-1-yloxytripyrrolidinophosphonium hexafluorophosphate), which facilitates the amidation reaction between cysteine and citrate (*31*). We proposed that the DNFC strategy could have a high potential in the fluorescence staining of large-scale tissues because the mild reaction conditions in DNFC can minimize the damage of biological molecules, and small citrate molecules can rapidly penetrate the thick tissues and specifically generate bright fluorophores on N-terminal cysteine with both free amine and thiol groups (Fig. 1A). Thus, we applied DNFC to thick tissue samples and examined the compatibility of the existing tissue clearing techniques to observe the general morphology of cleared tissues with minimal deformation.

It was suggested that the TPA formation starts from the carboxylic group activation of citrate by PyBOP in the DNFC staining (fig. S1). Then, the primary amine group of N-terminal cysteine attacks the activated carboxylic group to form the amide bond. Slight basic conditions using an organic base, *N,N*-diisopropylethylamine (DIPEA), were preferred to deprotonate citrate and cysteine for promoting the amide formation as the standard peptide synthesis reaction using PyBOP. After serial dehydration reactions, the TPA structure can be formed on the N-terminal cysteine. To optimize the DNFC protocol for 3D tissue imaging, we conducted several experiments to facilitate fluorophore generation. Because of the dehydration to complete TPA formation, low water environment is favored (*25*–*31*). Therefore, a serial exchange of dehydration solutions was performed to minimize possible tissue deformation. For the tissue clearing technique, we selected 3DISCO, an organic solvent-based tissue clearing method, due to the dehydrated reaction conditions of DNFC. In a previous report, tetrahydrofuran (THF) was used as a tissue dehydrant in 3DISCO (*6*). However, significantly higher fluorescence intensity was obtained when *N,N*-dimethylformamide (DMF) was used as the dehydrant instead of THF. Thus, we adopted a DMF-based dehydration process for tissue staining and clearing (fig. S2A).

After dehydration, citrate, DIPEA, and PyBOP were added to the samples for fluorophore generation. Facilitated by PyBOP, the TPA structure is formed through successive amide/imide couplings between citrate and N-terminal cysteines of peptides or proteins. The fluorophore was gradually generated according to the incubation time until 24 hours (fig. S2B); however, the temperature (room temperature versus 37°C) did not significantly affect fluorophore generation (fig. S2C). Therefore, we selected the incubation time and temperature as 24 hours and room temperature for further experiments. The TPA fluorophore has a maximum emission at 450 nm by excitation at a maximum absorption wavelength of 370 nm (*31*). In this study, we selected to excite TPA at 405 nm, the wavelength of a blue laser in conventional confocal microscopy. Given this condition, TPA exhibits a broad spectrum with a maximum emission of approximately 500 nm (*31*). The DNFC-stained tissue sample showed a similar fluorescence spectrum with excitation at 405 nm, which supports that TPA can be successfully generated in biological samples (fig. S3). To verify that citrate forms fluorophores on the N-terminal cysteines of peptides or proteins, cells were pretreated with *N*-ethylmaleimide, a thiol capping reagent. Fluorescence generation was significantly inhibited in this condition, and there was only negligible fluorescence without significant differences from nonstained cells (fig. S4). These results strongly suggest that the strong fluorescence in DNFC-stained biological samples is closely related to TPA generation from citrate and N-terminal cysteine.

Following dehydration and DNFC staining, RI homogenization using benzyl alcohol-benzyl benzoate (BABB) was performed to reduce light scattering in thick biological samples (*6*, *7*, *32*, *33*). Figure 1B shows images of whole mouse kidneys before and after DNFC staining and tissue clearing. The DNFC-processed kidneys became transparent after RI matching and emitted bright fluorescence under ultraviolet (UV) light. The results showed that the DNFC was successfully combined with 3DISCO. We found that DNFC with tissue clearing revealed the structural information of the kidney with a much higher fluorescence emission than that of the nontreated sample (Fig. 1C). In addition, 3DNFC increased the signal intensity of stained tissues and formed fluorophores on proteins via a covalent bond, allowing the observation of detailed structures. In their optical section images, the characteristic structure of the kidney, i.e., podocytes, tubules, and glomerulus, can be observed at cellular resolution without further labeling (Fig. 1D). The image based on the autofluorescence barely showed the detailed structure even after a fivefold enhancement of the brightness and the contrast. Compared to the autofluorescence of the nonprocessed tissue, the emission intensity of the 3DNFC-processed kidney increased by more than 40-fold through fluorophore formation (Fig. 1E).

After successfully combining DNFC with cleared tissue imaging, we termed this tissue labeling-clearing process as 3DNFC. 3DNFC, the integration of citrate-based fluorogenic reaction and tissue clearing techniques, can be applied to stain thick tissue specimens and provide the morphological features and detailed structures of tissues at the cellular level.

Versatile labeling and imaging of various tissues by 3DNFC

We applied the 3DNFC strategy to various mouse tissue samples to confirm its versatility for tissue imaging. 3DNFC processing successfully showed structural features in various tissues such as the brain, lung, liver, adipose tissue, tongue, esophagus, intestine, and ovary (Fig. 2A). In the brain, molecular cell and granular layers were clearly distinguished through the 3DNFC process. Ciliated cells in the bronchus and alveoli were clearly visualized in the lungs. The 3DNFC-processed liver showed a large contrast between the hepatocytes and sinusoids or veins. 3DNFC provided morphological and

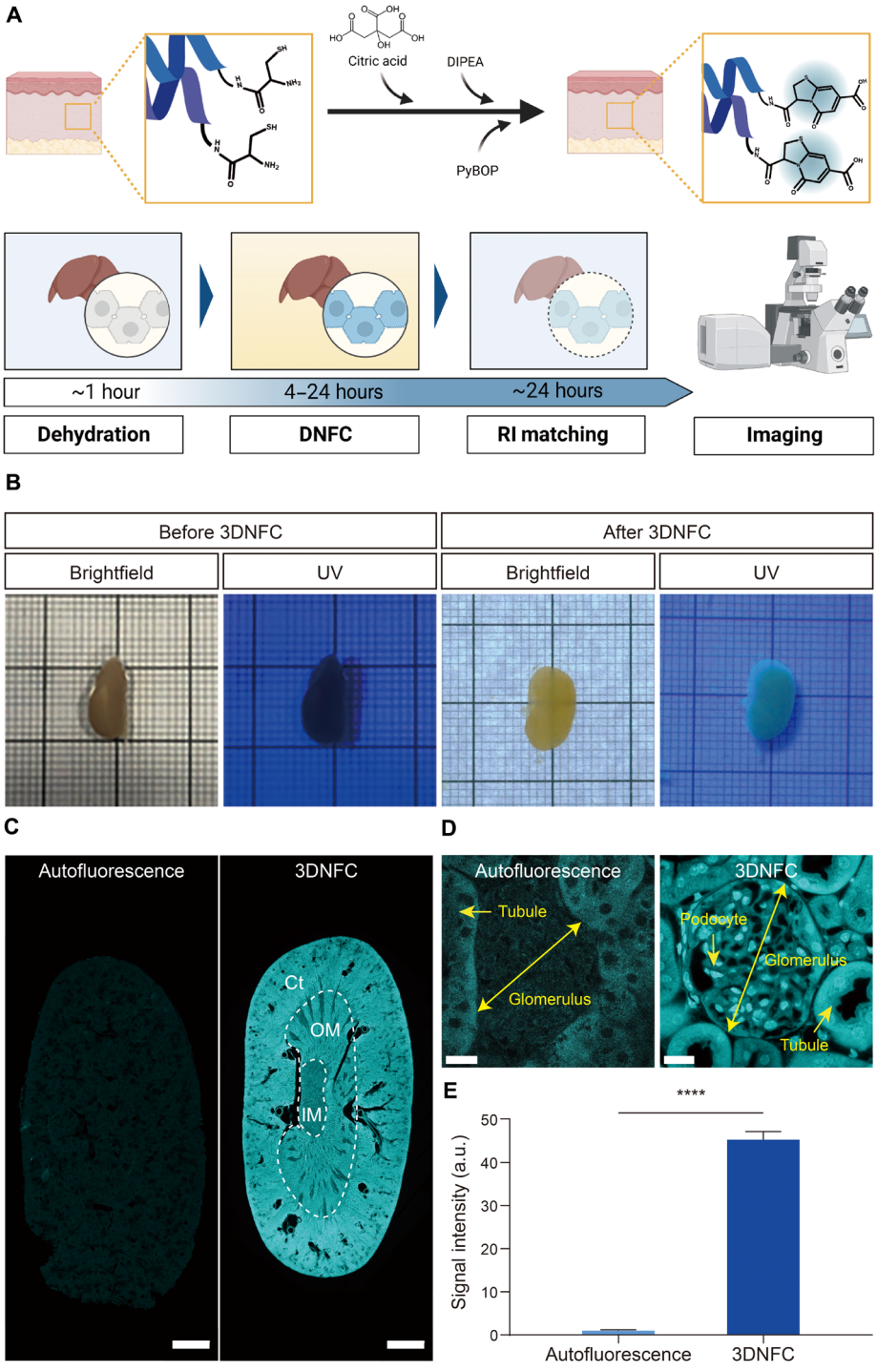

Fig. 1. 3DNFC reveals the anatomical features of tissues through the integration of citrate-based fluorophore formation and tissue clearing techniques. (**A**) Schematic illustration of the 3DNFC. 3DNFC is the integration of two techniques, the DNFC staining technique that forms fluorophores in a de novo manner on the N termini of peptides or proteins and the tissue clearing technique that makes tissues transparent. 3DNFC is conducted in the following orders: dehydration, fluorophore formation, RI matching, and imaging. (**B**) Whole mouse kidney before and after the 3DNFC. Before the 3DNFC, the kidney was opaque and showed no strong fluorescence emission under ultraviolet (UV) light. Besides, the 3DNFC-processed kidney becomes transparent and fluorescent under UV light. (**C**) Images of nonprocessed and 3DNFC-processed kidney slices. The 3DNFC-processed kidney emits strong cyan fluorescence throughout the whole tissue and shows the distinct structures in the cortex (Ct), outer medulla (OM), and inner medulla (IM). Scale bars, 1 mm. (**D**) Optical section images of the nonprocessed and 3DNFC-processed kidney. The brightness and the contrast in the image of the nonprocessed sample were enhanced by more than fivefold for the observation of the microstructure due to the weak autofluorescence. On the other hand, the 3DNFC-processed kidney achieves the cellular resolution imaging of the kidney glomerulus without such enhancement. Scale bars, 20 μm. (**E**) Comparison of the fluorescence intensity from the confocal laser scanning microscopy (CLSM) images of nonprocessed and 3DNFC-processed kidney samples. Data are shown as means ± SEM ($n = 9$). ****$P < 0.0001$. All DNFC fluorescence was obtained by collecting emission between 410 and 600 nm with an excitation at 405 nm. a.u., arbitrary units.

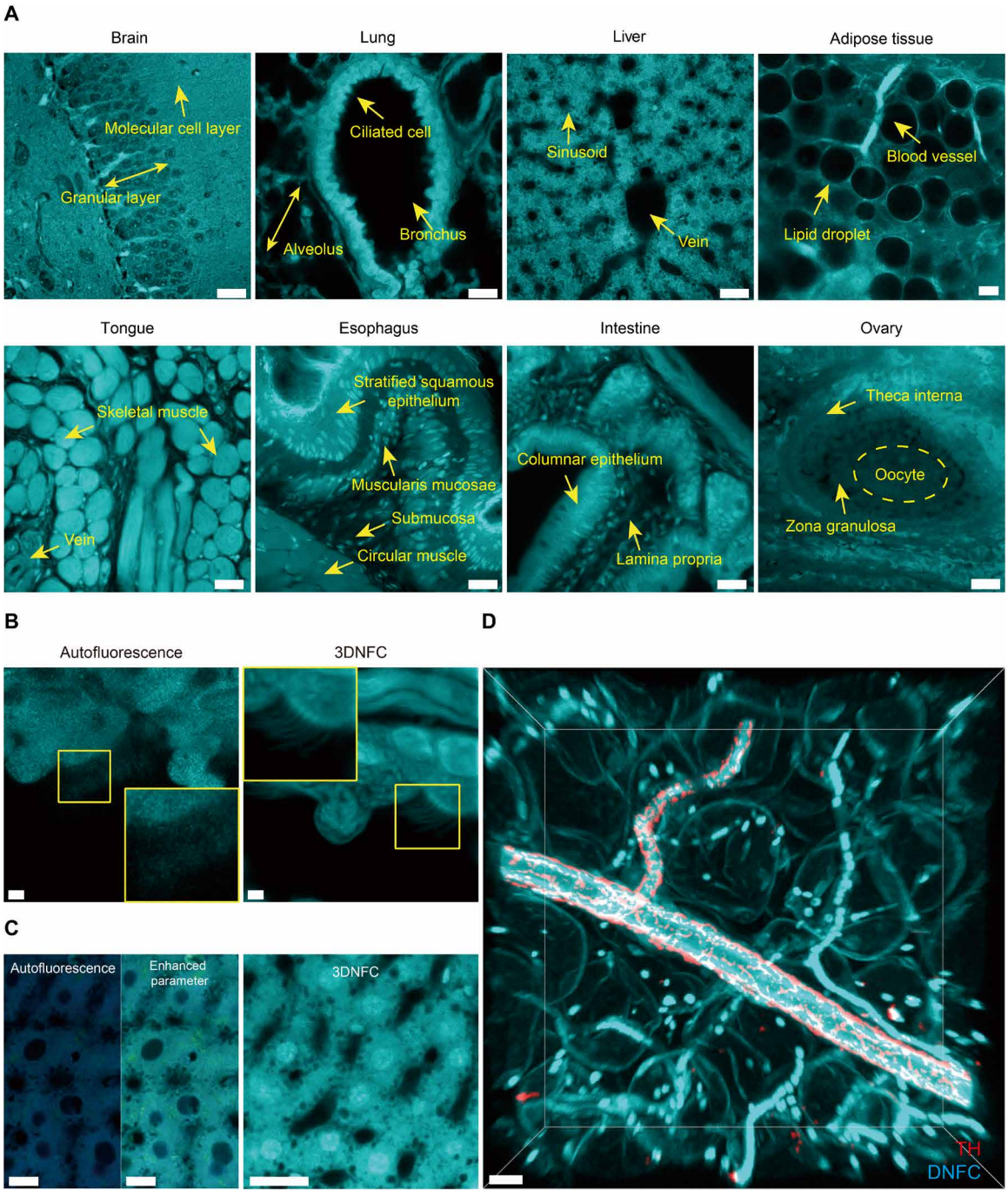

Fig. 2. 3DNFC allows versatile imaging in a wide variety of tissues with enhanced contrast. (**A**) Optical section images of various 3DNFC-processed mouse organ acquired with CLSM. Scale bars, 25 μm (brain, lung, liver, tongue, esophagus, intestine, and ovary) and 50 μm (adipose tissue), respectively. (**B**) Observation of microstructures in the optical section images of lung. Mouse lung tissue was 3DNFC-processed and compared with the nonprocessed tissue (autofluorescence). The brightness and the contrast in the image of the nonprocessed sample were greatly enhanced due to the weak autofluorescence. The area in the box was magnified to show the detailed structure of cilia in the lung. Scale bars, 3 μm (autofluorescence) and 2 μm (3DNFC), respectively. (**C**) Observation of the microstructures in the optical section images of liver. Mouse liver tissue was 3DNFC-processed and compared with the nonprocessed tissue (autofluorescence). The CLSM images of nonprocessed tissue before and after the enhancement of the brightness and the contrast are shown. Scale bars, 15 μm (autofluorescence) and 25 μm (3DNFC), respectively. (**D**) Costaining of mouse adipose tissue with 3DNFC and fluorescence-labeled antibodies. The DNFC-stained adipose tissue was further stained with Alexa Fluor 647–labeled tyrosine hydroxylase (TH) antibody (red). The red fluorescence was obtained by collecting emission over 633 nm with an excitation at 633 nm. Scale bar, 30 μm. All DNFC fluorescence was obtained by collecting emission between 410 and 600 nm with an excitation at 405 nm. The thickness of all the tissue samples in the figure is 100 μm.

spatial information of adipocytes, which were observed as thin hollow spherical shells due to nonstained lipid droplets with minimal amounts of proteins and the blood vessels in the tissues (movie S1). The muscle layers and veins of the tongue, esophagus, and intestine were visualized using 3DNFC. In the ovary, the 3DNFC showed a granular structure and an oocyte. These data show the versatility of 3DNFC for tissue imaging. Other organs were also successfully cleared and fluorescently stained (fig. S5).

Through the generation of fluorescence in the tissues, 3DNFC reveals the tissue microstructures. Although autofluorescence showed blurred images of lung structure due to the low signal-to-background ratio, the 3DNFC-processed lung visualized its microstructures, i.e., respiratory epithelium including pulmonary cilia, with enhanced signal intensity (Fig. 2B). Furthermore, we found that the cell nuclei were fluorescently visualized only in the 3DNFC-processed tissue sections, not in the nonprocessed ones, as shown in the hepatocytes in the liver sample (Fig. 2C).

Multichannel imaging is required for the simultaneous spatial analysis of multiple targets of interest in tissue imaging. Because the 3DNFC process generates fluorescence with a broad spectrum of 430 to 600 nm (fig. S3), chemical dyes with red or far-red spectral fluorophores can be combined with the 3DNFC. Figure 2D shows the 3D rendering of adipose tissues stained with DNFC. Adipocytes in 3DNFC-processed adipose tissue were visualized as hollow spherical shapes. In addition, we visualized sympathetic nerves surrounding the blood vessels using fluorophore-labeled tyrosine hydroxylase antibodies (*34*). Combining 3DNFC and immunohistochemistry can reveal both general anatomical information and specific targets of specimens through multichannel imaging.

Together, 3DNFC can be applied to a wide variety of tissues and simultaneously enables the observation of general tissue morphologies and their microstructures. 3DNFC also achieves simultaneous analysis of diverse target of interests combined with other staining methods.

3D imaging and analysis of 3DNFC-processed tissues

Considering that the fluorescence of whole organs can be effectively enhanced by the 3DNFC process (fig. S5), we believed that 3D imaging of thicker tissues can be accomplished with confocal microscopy with a longer working distance. We applied the 3DNFC process to the whole lung lobe of the mice for 3D reconstruction and volumetric analysis. As a result, the structure of the entire lung lobe of a mouse was 3D reconstructed (Fig. 3A and movie S2). The structures of the segmental bronchi and alveoli were observed in the optical section images of the 3D-reconstructed lung lobe (Fig. 3B). Moreover, we could perform various quantitative analyses of the 3DNFC-processed tissues because the 3DNFC provides the morphological and spatial information of the biological samples in a 3D manner. For example, we analyzed red blood cells (RBCs) in spleen tissue sections. We acquired optical section images of the red pulp in 3DNFC-processed spleen tissues and reconstructed the 3D images (Fig. 3C and movie S3). After costaining with an RBC-targeting antibody and nucleus-targeting SYTO 82 dye (fig. S6), we verified that the biconcave structures shown in the 3D-reconstructed images were RBCs in the spleen. 3DNFC-based multichannel imaging can provide the general morphology of the spleen tissue (DNFC) and the distribution of RBCs (antibody) and other cells (SYTO 82). Furthermore, we obtained various quantitative information from the 3D-reconstructed image, such as the membrane surface area and sphericity of RBCs, which are related to the RBC membrane disorders such as hereditary spherocytosis and elliptocytosis (*35*, *36*). Decreased deformability of the RBC membrane can cause premature removal of RBC in the spleen, resulting in hemolytic anemia (*37*, *38*). 3D-reconstructed images provide the number of RBCs per volume and the volumetric ratio of RBCs in the spleen, which are also associated with such diseases (*39*).

Quantitative and histopathological analyses of the 3DNFC-processed liver tissue

After confirming the possibility of the 3DNFC process for the 3D reconstruction of tissue morphology and quantitative analysis of cellular components, we envisioned that 3DNFC could be used as a 3D version of H&E in histopathological examination. To test this potential, we applied the 3DNFC to analyze pathological features in NAFLD, a complex liver disease with an accumulation of excess fat in the liver due to diabetes or obesity (*40*). NAFLD is the most common liver disorder; approximately 25% of the world's population suffers from NAFLD. NAFLD was induced in mice by feeding a high-fat diet (HFD) consisting of 60% fat in a meal for 6 weeks and 6 months (*41*, *42*). Mouse liver tissues were harvested and serially sectioned with a thickness of 4 μm. Each consecutive slide was stained with H&E or 3DNFC/propidium iodide (PI) for direct comparison (fig. S7). DNFC and PI staining showed the nuclei and cytoplasmic compartments of hepatocytes, respectively, which corresponded to H&E in the H&E staining. Around the hepatocytes, lipid vacuoles were observed in both the H&E and 3DNFC images. Moreover, we found that the density of lipid droplets increased in liver tissue between 6 weeks and 6 months. As shown in Fig. 2A, lipid droplets were not stained through the 3DNFC process and are shown as voids in the image. We compared the 3DNFC-processed tissue image with the tissue image stained with Nile Red, a lipid staining dye (Fig. 4A). Because of the delipidation during the 3DNFC process, the multiplex imaging of Nile Red–stained lipids and DNFC-labeled proteins is difficult to achieve. Nonetheless, results indicate that the distribution of dark hollow spheres in the 3DNFC image could be matched with the distribution of the red fluorescence in the Nile Red–stained image (fig. S8).

Although the sectional images of the liver tissue slides provided important pathological information for NAFLD development, we obtained more detailed information from the 3D-reconstructed images of 3DNFC-processed tissues. On the basis of the 3DNFC-staining features of lipid droplets, we defined the unstained dark hollow spheres as the lipid droplets and obtained various quantitative volumetric information from the NAFLD tissues (Fig. 4B). In the 100-μm-thick high fat–induced fatty liver tissue, we could visualize the 3D distribution of the lipid droplets (movies S4 and S5). Compared with the tissue at 6 weeks, the size of the lipid droplets was much larger at 6 months. The size distribution histograms at the two time points are compared in Fig. 4C. The lipid droplets at 6 months showed a much broader size distribution, with a marked increase in the average size compared to those at 6 weeks. At 6 weeks, 94% of the lipid droplets were smaller than 10 μm in diameter. In addition, the ratio of lipid droplets larger than 10 μm in diameter was 78% at 6 months. The average diameter of lipid droplets increased more than twofold between 6 weeks and 6 months, indicating the development of NAFLD in the mouse model. In addition to the size distribution, we calculated the number of lipid droplets per volume, volumetric portion, and sphericity of the lipid droplets in the tissue, which cannot

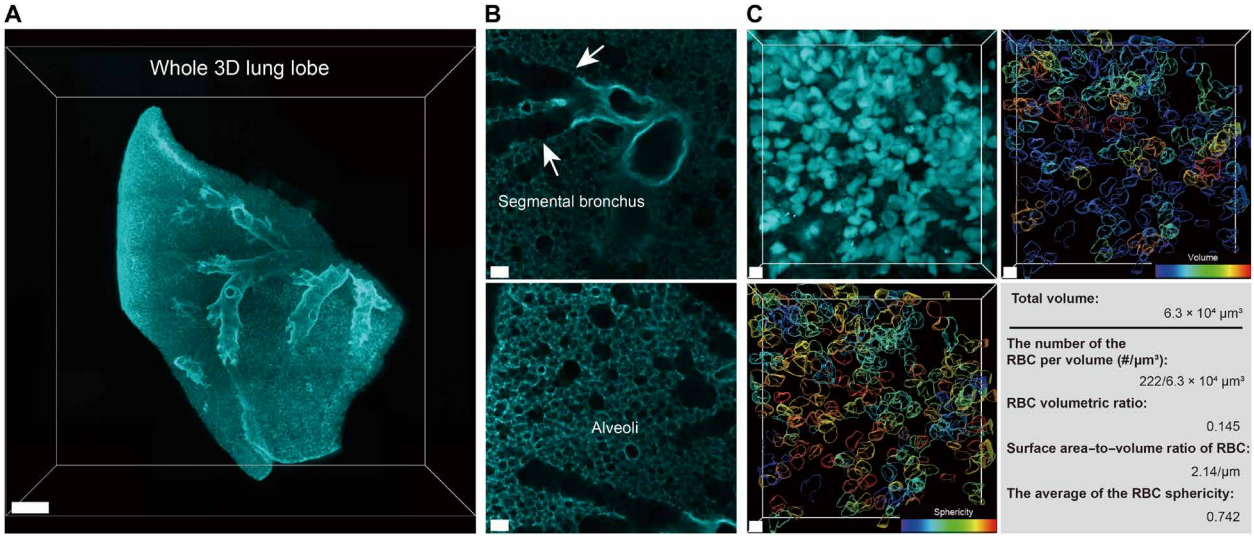

Fig. 3. 3DNFC enables 3D optical imaging and the volumetric analysis of large-scale tissue. (**A**) 3D rendering of 3DNFC-processed whole mouse lung lobe acquired with CLSM. Structural features of the lung, i.e., segmental bronchus, alveoli, are observed in the images. Scale bar, 400 μm. (**B**) Optical section images from the 3D-reconstructed whole lung lobe of mouse. Scale bars, 70 μm. For the analysis, a mouse whole lung lobe was 3DNFC-processed with 24-hour DNFC staining and 24-hour RI homogenization. (**C**) 3D reconstruction of RBCs in the 3DNFC-processed spleen tissue and quantified volumetric information and sphericity of RBCs from the 3DNFC-proccessed spleen tissue. The color bar of the image indicates their volume and sphericity. The thickness of the lung and spleen tissue sample in (B) and (C) is 100 μm. All the DNFC fluorescence was obtained by collecting emission between 410 and 600 nm with an excitation at 405 nm.

be precisely obtained using 2D histochemistry. The number of lipid droplets per volume decreased slightly during this period but not significantly due to the high SD (Fig. 4D). In contrast, the volumetric portion of lipid droplets in the liver tissue increased approximately 20-fold during the period (Fig. 4E). The marked increase in the volumetric portion during NAFLD development is consistent with previous reports (*43*). The sphericity of the lipid droplets slightly but significantly decreased with NAFLD development (Fig. 4F). The significant increase in the size and volumetric portion but the slight decrease in the number density and sphericity may imply possible fusion of the lipid droplets during the period (*43*). 3DNFC enables the analysis of each pathological property of NAFLD in a 3D manner. These results support the potential application of 3DNFC in the 3D visualization of clinical tissues with quantitative analysis of various pathological features.

Volumetric analysis of human clinical samples

Last, we applied the 3DNFC to human clinical samples to observe the substructures of pathological tissues in a 3D manner, which appeared to be challenging in conventional slide-based histology. We first compared consecutive sections of human breast cancer tissue after H&E staining and 3DNFC processing for direct comparison. PI is simultaneously used in the 3DNFC process to counterstain cell nuclei, which could substitute nucleus-targeting hematoxylin in H&E staining. The PI and 3DNFC fluorescence in the 3DNFC-processed sectional image were in accordance with H&E colors in the H&E-stained image (Fig. 5A and fig. S9). The tumor cells were densely packed in the cancer tissue, and irregular adipocytes in the breast tissue were also observed as the voids in the 3DNFC-processed sectional image. The 3DNFC image shows the characteristic features of tumor tissues and enables the certification of the tumor lesion in the specimen, in accordance with the H&E images. Cribriform patterns with poorly formed glands were easily assigned in tumor areas with a high density of tumor cells (Fig. 5B). Furthermore, the 3DNFC image clearly distinguishes between tumor cells and stromal cells in the invasive front area of the tumor, which has a relatively low density of tumor cells. Combined with PI staining, 3DNFC-processed tumor tissue showed prominent nucleoli and 2.5-fold enlarged nuclei of cancer cells compared to diameters of erythrocytes (Fig. 5C). On the basis of the histopathological analysis of the H&E-stained tissue, the breast cancer in our study was assigned as grade 3 according to Nottingham histologic score system, indicating poorly differentiated carcinoma. In analyzing the tumor area structures in the 3DNFC images, breast cancer was confirmed as at least grade 2, indicating moderately differentiated carcinoma or more. If we could obtain information on a mitotic count in cancerous tissues by other nucleus staining methods, then we could further improve the accuracy of 3DNFC-based diagnosis and prognosis.

Understanding spatial heterogeneity in the tumor area is essential in the prognosis and diagnosis of cancer and in basic and clinical cancer biology (*44*, *45*). However, because the microscopic analysis of H&E-stained slides provides only 2D information, repeated observation of the number of consecutive slides is required to obtain 3D information. In this experiment, we applied 3DNFC to the breast cancer tissue and obtained a 3D-reconstructed image of the 100-μm-thick tissue through volumetric imaging (Fig. 5D). The 3D visualization of the tumor showed an uneven distribution of tumor cells according to the imaging depth (Fig. 5E) Moreover, we could observe the formation of vascular channels surrounding a tumor cluster in the 3D-reconstructed images (movie S6). Together, our results demonstrate the successful application of 3DNFC as a 3D analog of H&E staining for histopathological diagnosis.

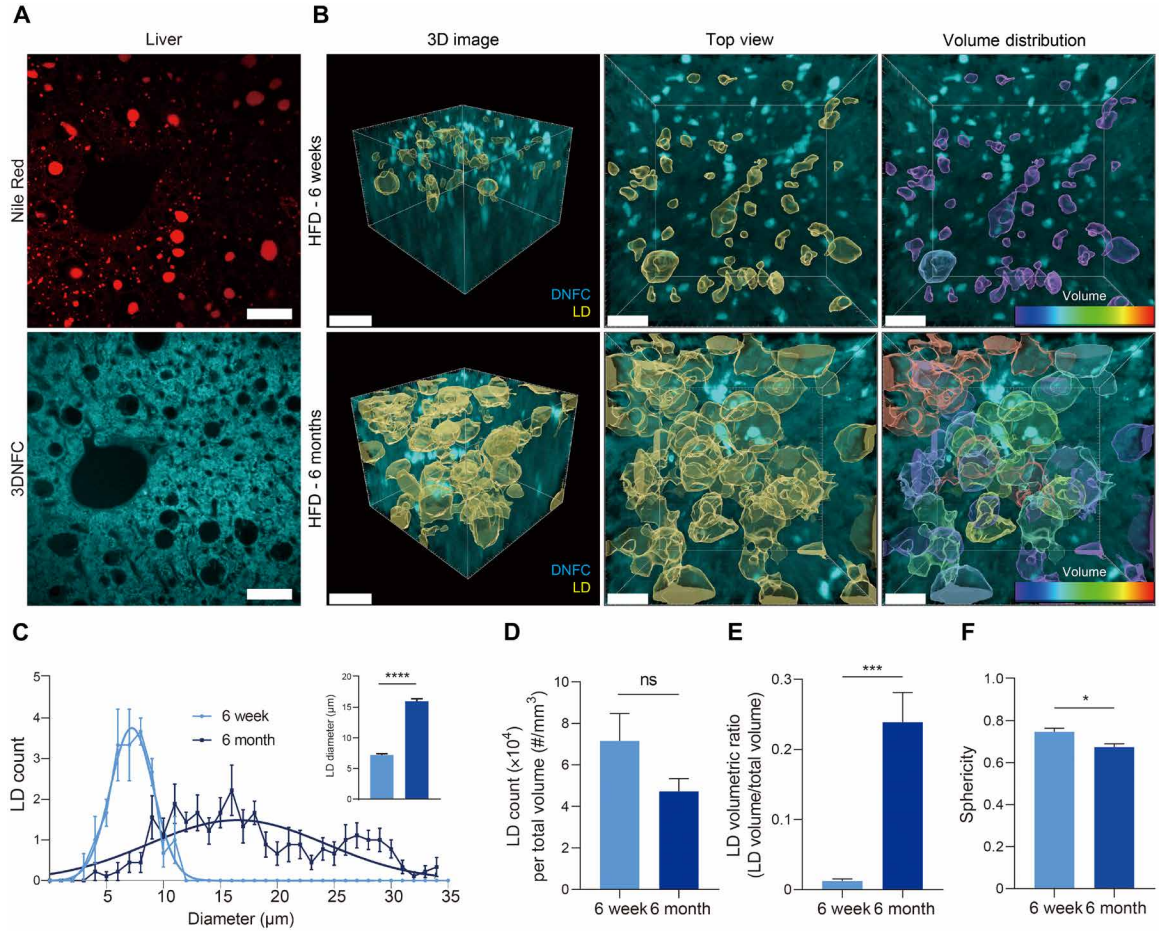

Fig. 4. Analyses of 3DNFC-processed liver tissue of mice with NAFLD. (**A**) Visualization of lipid droplets in Nile Red–stained and 3DNFC-processed mouse liver tissue samples. A 100-μm-thick mouse spleen tissue sample was stained with Nile Red (red). The sample was destained and restained by the 3DNFC protocol. The red and cyan fluorescence signals were obtained by collecting emission between 539 and 753 nm and 410 and 600 nm by excitation at 514 and 405 nm, respectively. The dark hollow spheres in the 3DNFC image are well matched to the red fluorescence in the Nile Red–stained image. Scale bars, 50 μm. (**B**) 3D rendering and 3D-reconstructed images of lipid droplets in the liver tissues of the NAFLD-induced mice. The color bars of the images represent the volume of the lipid droplet. Scale bars, 30 and 20 μm in the 3D rendering and the 3D-reconstructed images, respectively. (**C**) Distribution of diameters of lipid droplets in the liver tissues. In each distribution, the curve indicates the Gaussian fitting. The inset compares the average diameters of the liver tissues from mice fed with HFD for 6 weeks and 6 months. Comparison of (**D**) the number density, (**E**) the volumetric portion, and (**F**) the sphericity of the lipid droplets in the liver tissues from the NAFLD-induced mice. All the data are shown as means ± SEM ($n = 7$ for 6 weeks and $n = 8$ for 6 months). (*), (***), (****), and n.s. indicate $P < 0.05$, $P < 0.001$, $P < 0.0001$, and no significant difference by the Mann-Whitney test, respectively. All the DNFC fluorescence was obtained by collecting emission between 410 and 600 nm with an excitation at 405 nm.

DISCUSSION

2D histopathology provides morphological information on the lesion for diagnosis and prognosis (*46*). However, tissue slide processing in 2D histopathology is inevitably accompanied by the loss of volumetric information. Recently, fluorescence-based imaging with tissue clearing techniques has been highlighted because it enables us to obtain detailed 3D structures of clinical tissue samples (*6*, *10*, *47*). Nevertheless, slow penetration of antibodies into thick tissues (*17*, *18*) and nonspecific binding of chemical fluorescent dyes, as well as the instability of the noncovalent fluorescent labeling during the tissue clearing process, may decrease the analytic accuracy (*19*, *20*). Chemical fluorophores with reactive functional groups enable covalent labeling on biomolecules for observation of the general morphology of tissues and spatial distribution of the biomolecules (*5*). However, the relatively high cost of the reactive dyes limits their availability in large-scale tissue imaging. The label-free imaging based on autofluorescence (*22*) or clearing-enhanced stimulated Raman scattering microscopy has been suggested to overcome these limitations in fluorescence staining (*48*). However, autofluorescence-based tissue imaging requires high-power laser excitation, causing sample deformation due to the weak emission intensity (*23*), and clearing methods for the 3D-Raman spectroscopy should be more improved for high-quality imaging (*48*). Therefore, fluorescence imaging techniques without these restrictions in the staining or imaging of thick tissues are still required for accurate and effective analyses of pathological tissues. To fill this need, we developed and presented 3DNFC, in which the fluorescence intensity of tissues can be enhanced by a simple fluorogenic reaction using citrate (Fig. 1).

The enhancement of fluorescence intensity in 3DNFC is achieved by the generation of the TPA fluorophore (*31*). Unlike other chemical fluorophores, TPA can be covalently conjugated on the N-terminal cysteine of peptides or proteins during the fluorophore generation

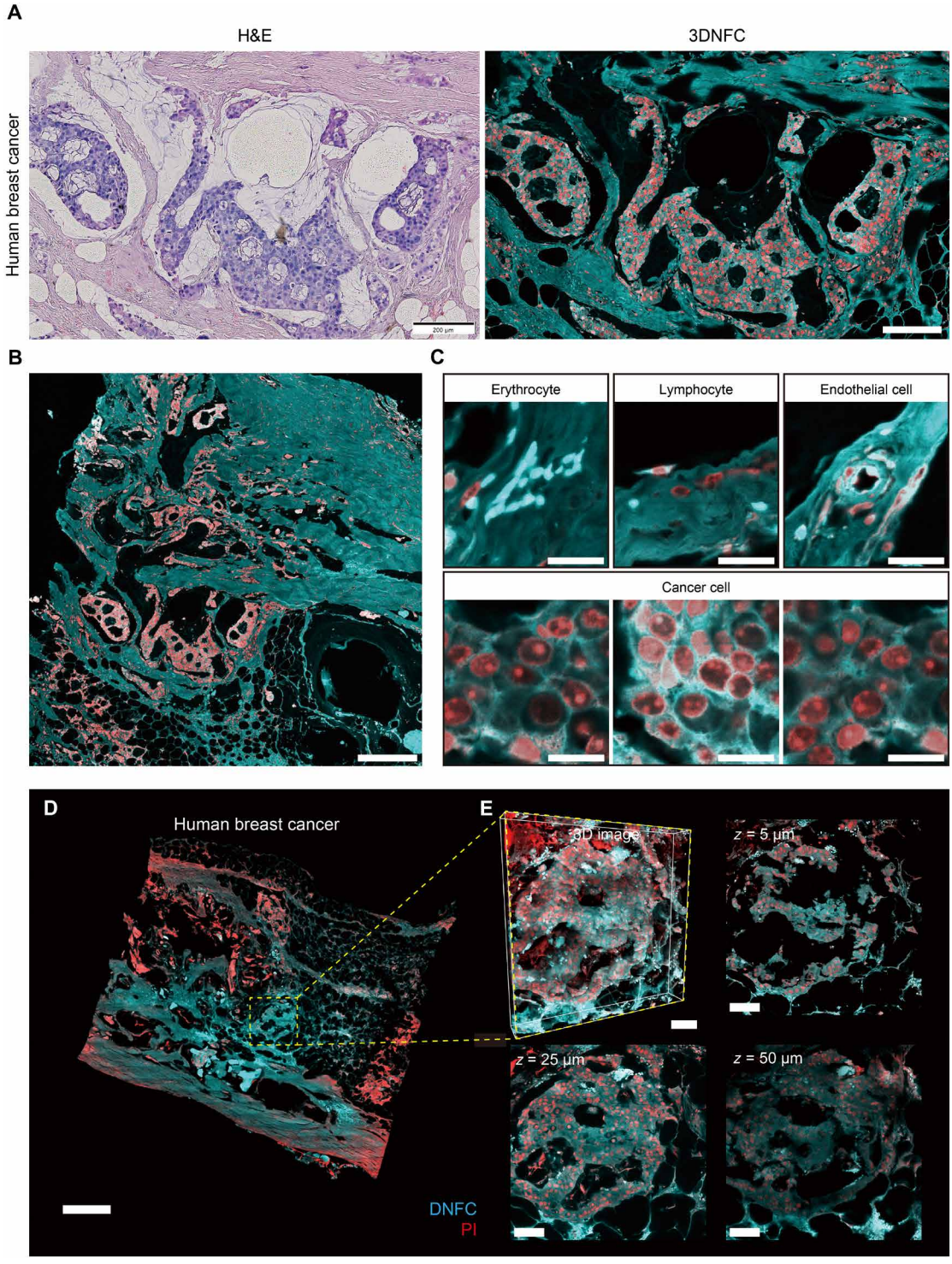

Fig. 5. Volumetric imaging and analysis of 3DNFC-processed human breast cancer tissues. (**A**) Comparison of human derived breast cancer tissues, which were stained by the 3DNFC process or by the conventional H&E staining. Two consecutive slices with a thickness of 4 μm were obtained by serial microsectioning of the formalin-fixed, paraffin-embedded cancer tissue. Scale bars, 200 μm. (**B**) A representative image of the 3DNFC-processed cancer tissue. Scale bar, 500 μm. (**C**) Magnified images of erythrocytes, lymphocytes, endothelial cells, and cancer cells in the 3DNFC-processed cancer tissue. Scale bars, 25 μm. (**D**) A representative CLSM section image of a 100-μm-thick human breast cancer tissue. Scale bar, 500 μm. (**E**) 3D rendering of the tumor core in the human breast cancer and the sectional images at multiple depths between 5 and 50 μm. Scale bars, 80 μm. All the DNFC fluorescence was obtained by collecting emission between 410 and 600 nm with an excitation at 405 nm. In the 3DNFC images, PI (red) was costained for the selective visualization of cell nuclei. The red fluorescence was obtained by collecting emission between 600 and 750 nm with an excitation at 543 nm.

from cost-effective nonfluorescent biomolecules, citrate. The 3DNFC process can show the morphology of various tissues at cellular resolution with improved fluorescence intensity and contrasts (Fig. 2). Owing to the covalent bond formation, 3DNFC is compatible with conventional tissue clearing techniques and achieves detailed volumetric analyses of tissues based on their 3D-reconstructed images (Fig. 3). Recently, 3D histology, in which multiple consecutive tissue slides are serially observed for the 3D reconstruction by spatial arrangement algorithms, has been developed (*49*–*55*). However, imaging hundreds of sectioned slides is time-consuming and laborious (*56*). In contrast, 3DNFC achieves deep tissue imaging with simplified sample preparation and faster volumetric imaging than slide-based 3D histology.

Several strategies have been tried to give diagnostic quality volumetric images of pathological tissues (*56*–*58*). For example, labeling biopsy samples with DRAQ5, the nucleus-staining dye, and eosin could generate images resembling the results of conventional H&E staining for 3D reconstruction (*56*, *57*). On the basis of these efforts, we applied 3DNFC to various pathological samples such as NAFLD and human breast cancer (Figs. 4 and 5). 3DNFC analyses of animal disease samples allowed the quantitative volumetric evaluation of pathological features in NAFLD tissues and tracking of the disease progress in a 3D manner (Fig. 4). Because TPA fluorophores are mainly generated on N-terminal cysteine of proteins, the staining gradient in 3DNFC-processed tissues might reflect the variation of N-proteome according to the subcellular structure. Therefore, a detailed analysis of N-proteome in normal and pathological samples with different DNFC staining intensities may reveal unknown pathological biomarkers. Furthermore, through the 3DNFC of human clinical samples on a large scale, we observed 3D spatial heterogeneity of the tumor mass and determined the grade of human breast cancer (Fig. 5). We have shown that 3DNFC enables the volumetric analysis of tumor shape and growth pattern, which cannot be achieved in slide-based imaging techniques in histology and histopathology.

3DNFC overcomes many limitations of slide-based histopathology by integration of the novel fluorogenic reaction and tissue clearing technique. However, 3DNFC is also not free from intrinsic limitations of fluorescence microcopy, such as longer scanning time compared to those of normal light microscopy used in the imaging of conventional H&E-stained samples. We expect that these limitations can be overcome by the combination between 3DNFC and other fluorescence modalities such as a light sheet microscope, which resolves axial section images with a large field of view for rapid acquisition of the volumetric information (*59*). Along with other complementary imaging techniques, 3DNFC can be versatilely applied in pathology and make essential foundations for future practical clinical research.

MATERIALS AND METHODS

Chemicals and reagents

Citric acid monohydrate was purchased from Samchun Chemical, Korea (C0778). PyBOP was purchased from BeadTech, Korea. DIPEA was purchased from Tokyo Chemical Industry (TCI), Japan (D1217). DMF (D1615) and THF (T1733) were obtained from Samchun Chemical, Korea. Benzyl alcohol (24122) and benzyl benzoate (W213802) were obtained from Sigma-Aldrich, USA. DRAQ5 (62254) and SYTO 82 (S11363) were obtained from Thermo Fisher Scientific, USA. Anti-tyrosine hydroxylase antibody (ab112), anti-rabbit immunoglobulin G H&L (Alexa Fluor 647; ab150075), and anti-hemoglobin subunit alpha antibody (EPR3608) were purchased from Abcam, UK. Dulbecco's modified Eagle's medium (DMEM), Dulbecco's phosphate-buffered saline (PBS), and fetal bovine serum (FBS) were purchased from WelGENE, Korea.

Cell culture

HeLa (human cervical cancer, Korean Cell Line Bank, KCLB no. 10002) cells were maintained at 37°C in the presence of 5% CO_2 in DMEM with 10% FBS before the DNFC staining.

Animals

All mice (C57BL/6J) (JAX stock no. 000664) were housed in a temperature- and a humidity-controlled room with a reverse 12 hour-light/12-hour dark cycle, with ad libitum access to chow food and water. All experimental protocols were approved by the Institutional Animal Care and Use Committee of the Seoul National University Boramae Hospital.

Harvesting of mouse tissues

The mice were anesthetized using isoflurane and perfused transcardially with 4% ice-cold paraformaldehyde (PFA) in PBS. Tissues were harvested and incubated in the same fixative solution overnight at 4°C with gentle shaking. The fixed tissues were sectioned into slices with various thicknesses using a vibrating microtome, and the slices were stored in PBS at 4°C until use.

3DNFC process

The tissue samples were transferred to a glass vial and added with the first dehydrating solution, DMF/water (1/3, v/v). After 30-min gentle shaking with an orbital shaker, the solution was exchanged with the second dehydrating solution, DMF/water (1/1, v/v). After another 30-min shaking, the solution was exchanged with the final dehydrating solution, DMF/water (3/1, v/v). After 30 min, the solution was exchanged with a solution containing citric acid monohydrate (200 mg) and DIPEA (162 μl) in 1 ml of a DMF/water mixture (7/3, v/v). PyBOP (496 mg) in DMF (2 ml) was added to the solution for facilitating the TPA formation. The glass vial was covered with aluminum foils and gently shaken for varying times (4 to 24 hours). After the reaction, the samples were washed with DMF (3×) and PBS (3×), respectively. Then, the RI of the sample was matched by incubation in BABB (benzyl alcohol:benzyl benzoate = 1:2). The RI-matched sample was mounted on a slide glass filled with BABB and sealed with a reusable adhesive (Blu Tack) before imaging with a Zeiss LSM 880 laser scanning microscope (W Plan-Apochromat 10×/0.5 M27 working distance (WD) = 3.7 mm and C-Apochromat 40×/1.2 W Corr FCS M27 objective lens).

Image processing and analysis

3D rendering and visualization of the volumetric images were performed using the Imaris software (Bitplane). The RBCs in the 3DNFC-processed spleen tissue were reconstructed using the surface tool. The RBCs were smoothed with a filter size of 1 μm, and the surface was semiautomatically reconstructed on the basis of a manually selected local threshold. For the reconstruction of the lipid droplets in the 3DNFC-processed liver tissue, the whole liver tissue was initially reconstructed using the surface tool, and the outer space of the reconstructed liver surface was defined as a new channel for calculating the lipid droplets. The new channel can be used for the reconstruction of lipid droplets.

The NAFLD mouse model

Formalin-fixed, paraffin-embedded mouse fatty liver blocks were previously harvested in Seoul National University Boramae Medical Center. Briefly, TLR knockout B6SJLF1/J mice were fed with rodent diet consisting of 60% fat (Research Diets, catalog no. D12492) for 6 weeks and euthanized at 12 weeks. CXCL5 knockout C57BL/6 mice were fed with the same diet for 6 months and euthanized at 32 weeks. Each harvested liver was paraffin-embedded through a standard process (dehydration-clearing-infiltration-embedding) after the 4% PFA fixation. The stored tissue was deparaffinized using xylene before the 3DNFC process.

The human breast cancer sample

Formalin-fixed, paraffin-embedded human breast cancer block was provided by the Department of Surgery in Seoul National University Boramae Medical Center (Institutional Review Board no. 30-2020-30). The information of the breast cancer tissue used in this study is as follows: sex (female), age (64), race (Korean), and Nottingham combined histologic grade (grade 3). The stored tissue was deparaffinized using xylene before the 3DNFC process.

Statistical analysis

All statistical analyses were performed with the GraphPad Prism 8 software. We generally not only used the Student's unpaired *t* test without indication but also used the Mann-Whitney *U* test depending on the experimental paradigm. *, **, ***, ****, and n.s. mean $P < 0.05$, $P < 0.01$, $P < 0.001$, $P < 0.0001$, and not significant, respectively. All data are expressed as the means ± SEM. *n* values are stated in figure legends. No statistics to determine sample size, blinding, or randomization methods were used.

SUPPLEMENTARY MATERIALS

Supplementary material for this article is available at https://science.org/doi/10.1126/sciadv.add9419

View/request a protocol for this paper from *Bio-protocol*.

REFERENCES AND NOTES

1. G. Goel, S. Rao, N. Khurana, A. K. Sarda, Solitary necrotic nodule of liver (SNNL): A report of two cases. *J. Clin. Diagn. Res.* **8**, 115–116 (2014).
2. R. Zhang, Y. Cao, Y. Li, Z. Liu, J. Wang, J. He, C. Zhang, X. Sui, P. Zhang, L. Cui, S. Li, MVFStain: Multiple virtual functional stain histopathology images generation based on specific domain mapping. *Med. Image Anal.* **80**, 102520 (2022).
3. Y. Xu, J. G. Pickering, Z. Nong, E. Gibson, J.-M. Arpino, H. Yin, A. D. Ward, A method for 3D histopathology reconstruction supporting mouse microvasculature analysis. *PLOS ONE* **10**, e0126817 (2015).
4. J. T. C. Liu, A. K. Glaser, K. Bera, L. D. True, N. P. Reder, K. W. Eliceiri, A. Madabhushi, Harnessing non-destructive 3D pathology. *Nat. Biomed. Eng.* **5**, 203–218 (2021).
5. C. Mao, M. Y. Lee, J.-R. Jhan, A. R. Halpern, M. A. Woodworth, A. K. Glaser, T. J. Chozinski, L. Shin, J. W. Pippin, S. J. Shankland, J. T. C. Liu, J. C. Vaughan, Feature-rich covalent stains for super-resolution and cleared tissue fluorescence microscopy. *Sci. Adv.* **6**, eaba4542 (2020).
6. A. Ertürk, K. Becker, N. Jährling, C. P. Mauch, C. D. Hojer, J. G. Egen, F. Hellal, F. Bradke, M. Sheng, H.-U. Dodt, Three-dimensional imaging of solvent-cleared organs using 3DISCO. *Nat. Protoc.* **7**, 1983–1995 (2012).
7. E. A. Susaki, K. Tainaka, D. Perrin, F. Kishino, T. Tawara, T. M. Watanabe, C. Yokoyama, H. Onoe, M. Eguchi, S. Yamaguchi, T. Abe, H. Kiyonari, Y. Shimizu, A. Miyawaki, H. Yokota, H. R. Ueda, Whole-brain imaging with single-cell resolution using chemical cocktails and computational analysis. *Cell* **157**, 726–739 (2014).
8. K. Chung, J. Wallace, S.-Y. Kim, S. Kalyanasundaram, A. S. Andalman, T. J. Davidson, J. J. Mirzabekov, K. A. Zalocusky, J. Mattis, A. K. Denisin, S. Pak, H. Bernstein, C. Ramakrishnan, L. Grosenick, V. Gradinaru, K. Deisseroth, Structural and molecular interrogation of intact biological systems. *Nature* **497**, 332–337 (2013).
9. J. Seo, M. Choe, S.-Y. Kim, Clearing and labeling techniques for large-scale biological tissues. *Mol. Cells* **39**, 439–446 (2016).
10. Y. Chen, Q. Shen, S. L. White, Y. Gokmen-Polar, S. Badve, L. J. Goodman, Three-dimensional imaging and quantitative analysis in CLARITY processed breast cancer tissues. *Sci. Rep.* **9**, 5624 (2019).
11. I. Sabdyusheva Litschauer, K. Becker, S. Saghafi, S. Ballke, C. Bollwein, M. Foroughipour, J. Gaugeler, M. Foroughipour, V. Schavelová, V. László, B. Döme, C. Brostjan, W. Weichert, H.-U. Dodt, 3D histopathology of human tumours by fast clearing and ultramicroscopy. *Sci. Rep.* **10**, 17619 (2020).
12. W. Sun, M. Li, J. Fan, X. Peng, Activity-based sensing and theranostic probes based on photoinduced electron transfer. *Acc. Chem. Res.* **52**, 2818–2831 (2019).
13. M. Tian, Y. Ma, W. Lin, Fluorescent probes for the visualization of cell viability. *Acc. Chem. Res.* **52**, 2147–2157 (2019).
14. M. Gao, F. Yu, C. Lv, J. Choo, L. Chen, Fluorescent chemical probes for accurate tumor diagnosis and targeting therapy. *Chem. Soc. Rev.* **46**, 2237–2271 (2017).
15. X. Song, X. Han, F. Yu, J. Zhang, L. Chen, C. Lv, A reversible fluorescent probe based on C=N isomerization for the selective detection of formaldehyde in living cells and in vivo. *Analyst* **143**, 429–439 (2018).
16. X. Li, X. Gao, W. Shi, H. Ma, Design strategies for water-soluble small molecular chromogenic and fluorogenic probes. *Chem. Rev.* **114**, 590–659 (2014).
17. S.-Y. Kim, J. H. Cho, E. Murray, N. Bakh, H. Choi, K. Ohn, L. Ruelas, A. Hubbert, M. McCue, S. L. Vassallo, P. J. Keller, K. Chung, Stochastic electrotransport selectively enhances the transport of highly electromobile molecules. *Proc. Natl. Acad. Sci. U.S.A.* **112**, E6274–E6283 (2015).
18. T. Ku, W. Guan, N. B. Evans, C. H. Sohn, A. Albanese, J.-G. Kim, M. P. Frosch, K. Chung, Elasticizing tissues for reversible shape transformation and accelerated molecular labeling. *Nat. Methods* **17**, 609–613 (2020).
19. M. Tian, J. Sun, Y. Tang, B. Dong, W. Lin, Discriminating live and dead cells in dual-color mode with a two-photon fluorescent probe based on ESIPT mechanism. *Anal. Chem.* **90**, 998–1005 (2018).
20. B. Lin, Y. Liu, X. Zhang, L. Fan, Y. Shu, J. Wang, Membrane-activated fluorescent probe for high-fidelity imaging of mitochondrial membrane potential. *ACS Sens.* **6**, 4009–4018 (2021).
21. Y.-S. Zeng, R.-C. Gao, T.-W. Wu, C. Cho, K.-T. Tan, Fluorescent probe encapsulated in SNAP-tag protein cavity to eliminate nonspecific fluorescence and increase detection sensitivity. *Bioconjug. Chem.* **27**, 1872–1879 (2016).
22. S. Bhattacharjee, S. Satwaha, K. Thornton, D. Scholz, Label-free imaging and optical characterization of tissues based on autofluorescence. *ACS Omega* **3**, 5926–5930 (2018).
23. S.-J. Bae, D.-S. Lee, V. Berezin, U. Kang, K.-H. Lee, Multispectral autofluorescence imaging for detection of cervical lesions: A preclinical study. *J. Obstet. Gynaecol. Res.* **42**, 1846–1853 (2016).
24. D. Li, W. Qin, B. Xu, J. Qian, B. Z. Tang, AIE nanoparticles with high stimulated emission depletion efficiency and photobleaching resistance for long-term super-resolution bioimaging. *Adv. Mater.* **29**, 1703643 (2017).
25. J. Yang, Y. Zhang, S. Gautam, L. Liu, J. Dey, W. Chen, R. P. Mason, C. A. Serrano, K. A. Schug, L. Tang, Development of aliphatic biodegradable photoluminescent polymers. *Proc. Natl. Acad. Sci. U.S.A.* **106**, 10086–10091 (2009).
26. W. Kasprzyk, S. Bednarz, D. Bogdał, Luminescence phenomena of biodegradable photoluminescent poly(diol citrates). *Chem. Commun.* **49**, 6445–6447 (2013).
27. W. Kasprzyk, S. Bednarz, P. Żmudzki, M. Galica, D. Bogdał, Novel efficient fluorophores synthesized from citric acid. *RSC Adv.* **5**, 34795–34799 (2015).
28. J. P. Kim, Z. Xie, M. Creer, Z. Liu, J. Yang, Citrate-based fluorescent materials for low-cost chloride sensing in the diagnosis of cystic fibrosis. *Chem. Sci.* **8**, 550–558 (2017).
29. J. Hu, J. Guo, Z. Xie, D. Shan, E. Gerhard, G. Qian, J. Yang, Fluorescence imaging enabled poly(Lactide-co-glycolide). *Acta Biomater.* **29**, 307–319 (2016).
30. Z. Xie, J. P. Kim, Q. Cai, Y. Zhang, J. Guo, R. S. Dhami, L. Li, B. Kong, Y. Su, K. A. Schug, J. Yang, Synthesis and characterization of citrate-based fluorescent small molecules and biodegradable polymers. *Acta Biomater.* **50**, 361–369 (2017).
31. D. Jung, D. Choi, C. Sim, Y. Kim, S. Kang, S. H. Nam, J. Jang, D. Kim, M. S. Chang, J.-U. Park, Y. Lee, De novo formation of citrate-based fluorophores on N-termini of peptides and proteins in cells and tissues. *Chem. Commun.* **56**, 74–77 (2020).
32. J. Geng, X. Zhang, S. Prabhu, S. H. Shahoei, E. R. Nelson, K. S. Swanson, M. A. Anastasio, A. M. Smith, 3D microscopy and deep learning reveal the heterogeneity of crown-like structure microenvironments in intact adipose tissue. *Sci. Adv.* **7**, eabe2480 (2021).
33. B. Lloyd-Lewis, F. M. Davis, O. B. Harris, J. R. Hitchcock, F. C. Lourenco, M. Pasche, C. J. Watson, Imaging the mammary gland and mammary tumours in 3D: Optical tissue clearing and immunofluorescence methods. *Breast Cancer Res.* **18**, 127 (2016).
34. X. Li, Z. Mao, L. Yang, K. Sun, Co-staining blood vessels and nerve fibers in adipose tissue. *J. Vis. Exp.* , e59266 (2019).
35. L. Da Costa, L. Suner, J. Galimand, A. Bonnel, T. Pascreau, N. Couque, O. Fenneteau, N. Mohandas; Society of Hematology and Pediatric Immunology (SHIP) group; French Society of Hematology (SFH), Diagnostic tool for red blood cell membrane disorders: Assessment of a new generation ektacytometer. *Blood Cells Mol. Dis.* **56**, 9–22 (2016).

36. I. Safeukui, P. A. Buffet, G. Deplaine, S. Perrot, V. Brousse, A. Ndour, M. Nguyen, O. Mercereau-Puijalon, P. H. David, G. Milon, N. Mohandas, Quantitative assessment of sensing and sequestration of spherocytic erythrocytes by the human spleen. *Blood* **120**, 424–430 (2012).
37. H. Li, L. Lu, X. Li, P. A. Buffet, M. Dao, G. E. Karniadakis, S. Suresh, Mechanics of diseased red blood cells in human spleen and consequences for hereditary blood disorders. *Proc. Natl. Acad. Sci. U.S.A.* **115**, 9574–9579 (2018).
38. G. Deplaine, I. Safeukui, F. Jeddi, F. Lacoste, V. Brousse, S. Perrot, S. Biligui, M. Guillotte, C. Guitton, S. Dokmak, B. Aussilhou, A. Sauvanet, D. Cazals Hatem, F. Paye, M. Thellier, D. Mazier, G. Milon, N. Mohandas, O. Mercereau-Puijalon, P. H. David, P. A. Buffet, The sensing of poorly deformable red blood cells by the human spleen can be mimicked in vitro. *Blood* **117**, e88–e95 (2011).
39. Q. Liu, J. Wang, J. Cui, Z. Yang, G. Du, A novel acute anemia model for pharmacological research in mice by compelled acute exercise. *Acta Pharmacol. Sin.* **30**, 1643–1647 (2009).
40. Z. Younossi, F. Tacke, M. Arrese, B. Chander Sharma, I. Mostafa, E. Bugianesi, V. Wai-Sun Wong, Y. Yilmaz, J. George, J. Fan, M. B. Vos, Global perspectives on nonalcoholic fatty liver disease and nonalcoholic steatohepatitis. *Hepatology* **69**, 2672–2682 (2019).
41. J. Zhang, H. Du, M. Shen, Z. Zhao, X. Ye, Kangtaizhi granule alleviated nonalcoholic fatty liver disease in high-fat diet-fed rats and HepG2 cells via AMPK/mTOR signaling pathway. *J. Immunol. Res.* **2020**, e3413186 (2020).
42. Y. Li, J. Hai, L. Li, X. Chen, H. Peng, M. Cao, Q. Zhang, Administration of ghrelin improves inflammation, oxidative stress, and apoptosis during and after non-alcoholic fatty liver disease development. *Endocrine* **43**, 376–386 (2013).
43. J. Moon, E. Kong, J. Lee, J. Jung, E. Kim, S. B. Park, P. Kim, Intravital longitudinal imaging of hepatic lipid droplet accumulation in a murine model for nonalcoholic fatty liver disease. *Biomed. Opt. Express* **11**, 5132–5146 (2020).
44. M. Dobosz, V. Ntziachristos, W. Scheuer, S. Strobel, Multispectral fluorescence ultramicroscopy: Three-dimensional visualization and automatic quantification of tumor morphology, drug penetration, and antiangiogenic treatment response. *Neoplasia* **16**, 1–13 (2014).
45. S. S.-Y. Lee, V. P. Bindokas, S. J. Kron, Multiplex three-dimensional mapping of macromolecular drug distribution in the tumor microenvironment. *Mol. Cancer Ther.* **18**, 213–226 (2019).
46. N. Avril, S. Sassen, R. Roylance, Response to therapy in breast cancer. *J. Nucl. Med.* **50**, 55S–63S (2009).
47. S. Nojima, E. A. Susaki, K. Yoshida, H. Takemoto, N. Tsujimura, S. Iijima, K. Takachi, Y. Nakahara, S. Tahara, K. Ohshima, M. Kurashige, Y. Hori, N. Wada, J. Ikeda, A. Kumanogoh, E. Morii, H. R. Ueda, CUBIC pathology: Three-dimensional imaging for pathological diagnosis. *Sci. Rep.* **7**, 9269 (2017).
48. M. Wei, L. Shi, Y. Shen, Z. Zhao, A. Guzman, L. J. Kaufman, L. Wei, W. Min, Volumetric chemical imaging by clearing-enhanced stimulated Raman scattering microscopy. *Proc. Natl. Acad. Sci. U.S.A.* **116**, 6608–6617 (2019).
49. K.-A. Norton, S. Namazi, N. Barnard, M. Fujibayashi, G. Bhanot, S. Ganesan, H. Iyatomi, K. Ogawa, T. Shinbrot, Automated reconstruction algorithm for identification of 3D architectures of cribriform ductal carcinoma in situ. *PLOS ONE* **7**, e44011 (2012).
50. R. Grothausmann, L. Knudsen, M. Ochs, C. Mühlfeld, Digital 3D reconstructions using histological serial sections of lung tissue including the alveolar capillary network. *Am. J. Physiol. Lung Cell. Mol. Physiol.* **312**, L243–L257 (2017).
51. N. Roberts, D. Magee, Y. Song, K. Brabazon, M. Shires, D. Crellin, N. M. Orsi, R. Quirke, P. Quirke, D. Treanor, Toward routine use of 3D histopathology as a research tool. *Am. J. Pathol.* **180**, 1835–1842 (2012).
52. T. Mertzanidou, J. H. Hipwell, S. Reis, D. J. Hawkes, B. Ehteshami Bejnordi, M. Dalmis, S. Vreemann, B. Platel, J. van der Laak, N. Karssemeijer, M. Hermsen, P. Bult, R. Mann, 3D volume reconstruction from serial breast specimen radiographs for mapping between histology and 3D whole specimen imaging. *Med. Phys.* **44**, 935–948 (2017).
53. S. Korehisa, T. Ikeda, S. Okano, H. Saeki, E. Oki, Y. Oda, M. Hashizume, Y. Maehara, A novel histological examination with dynamic three-dimensional reconstruction from multiple immunohistochemically stained sections of a PD-L1-positive colon cancer. *Histopathology* **72**, 697–703 (2018).
54. Y. Yagi, R. G. Aly, K. Tabata, A. Barlas, N. Rekhtman, T. Eguchi, J. Montecalvo, M. Hameed, K. Manova-Todorova, P. S. Adusumilli, W. D. Travis, Three-dimensional histologic, immunohistochemical, and multiplex immunofluorescence analyses of dynamic vessel co-option of spread through air spaces in lung adenocarcinoma. *J. Thorac. Oncol.* **15**, 589–600 (2020).
55. Y. Tolkach, S. Thomann, G. Kristiansen, Three-dimensional reconstruction of prostate cancer architecture with serial immunohistochemical sections: Hallmarks of tumour growth, tumour compartmentalisation, and implications for grading and heterogeneity. *Histopathology* **72**, 1051–1059 (2018).
56. A. K. Glaser, N. P. Reder, Y. Chen, E. F. McCarty, C. Yin, L. Wei, Y. Wang, L. D. True, J. T. C. Liu, Light-sheet microscopy for slide-free non-destructive pathology of large clinical specimens. *Nat. Biomed. Eng.* **1**, 0084 (2017).
57. K. N. Elfer, A. B. Sholl, M. Wang, D. B. Tulman, S. H. Mandava, B. R. Lee, J. Q. Brown, DRAQ5 and eosin ('D&E') as an analog to hematoxylin and eosin for rapid fluorescence histology of fresh tissues. *PLOS ONE* **11**, e0165530 (2016).
58. F. Fereidouni, Z. T. Harmany, M. Tian, A. Todd, J. A. Kintner, J. D. McPherson, A. D. Borowsky, J. Bishop, M. Lechpammer, S. G. Demos, R. Levenson, Microscopy with ultraviolet surface excitation for rapid slide-free histology. *Nat. Biomed. Eng.* **1**, 957–966 (2017).
59. H. R. Ueda, A. Ertürk, K. Chung, V. Gradinaru, A. Chédotal, P. Tomancak, P. J. Keller, Tissue clearing and its applications in neuroscience. *Nat. Rev. Neurosci.* **21**, 61–79 (2020).

Acknowledgments: We acknowledge S.-J. Koh of the Department of Internal Medicine and Liver Research Institute, Seoul National University College of Hospital, Seoul National University College of Medicine for providing fatty liver–induced mice and J. Kim of the Department of Surgery, Seoul National University Boramae Medical Center, Seoul National University College of Medicine for providing of human breast cancer samples. **Funding:** This work was supported by the National Research Foundation of Korea Grants (NRF- 2017M3A9E9072938 and NRF-2021R1A2C2004476). **Author contributions:** Conceptualization: J.P., D.-J.K., D.J., Y.C., and Y.L. Methodology: J.P., D.-J.K., and D.J. Investigation: J.P., D.-J.K., H.C., and M.C. Visualization: J.P., D.-J.K., H.C., and M.-H.C. Supervision: B.K., J.-U.P., S.-Y.K., and Y.L. Writing—original draft: J.P., D.-J.K., and M.-H.C. Writing—review and editing: B.K., J.-U.P., S.-Y.K., and Y.L. **Competing interests:** The authors declare that they have no competing interests. **Data and materials availability:** All data needed to evaluate the conclusions in the paper are present in the paper and/or the Supplementary Materials.

Submitted 14 July 2022
Accepted 29 September 2022
Published 16 November 2022
10.1126/sciadv.add9419